

# Coherent interference in the resonant dissociative electron attachment to carbon monoxide

Shan Xi Tian,<sup>1,\*</sup> Bin Wu,<sup>1</sup> Lei Xia,<sup>1</sup> Yong-Feng Wang,<sup>1</sup> Hong-Kai Li,<sup>1</sup> Xian-Jin Zeng,<sup>1</sup> Yi Luo,<sup>1,2</sup> and Jinlong Yang<sup>1</sup>

<sup>1</sup>*Hefei National Laboratory for Physical Sciences at the Microscale and Department of Chemical Physics,*

*University of Science and Technology of China, Hefei, Anhui 230026, China*

<sup>2</sup>*Department of Theoretical Chemistry and Biology, School of Biotechnology, Royal Institute of Technology, S-106 91, Stockholm, Sweden*

(Received 10 February 2013; published 15 July 2013; corrected 17 July 2013)

Dissociative electron attachment to carbon monoxide,  $e^- + \text{CO} \rightarrow \text{C} + \text{O}^-$ , at 9.5, 10.0, and 10.6 eV is investigated by using the anion velocity time-sliced map imaging technique. The completely backward scattering distributions of the fast  $\text{O}^-$  fragment are observed at 10.0 and 10.6 eV. The single electron-molecule resonance model fails in interpretation to these unusual angular distributions, while a quantum interference model including two (at 10.0 eV) or three (at 10.6 eV) dissociative outgoing waves is consequently proposed and provides the satisfying results about the experimental data fittings. Moreover, coherent interference among the  $^2\Pi$ ,  $^2\Delta$ , and  $^2\Phi$  resonant states of  $\text{CO}^-$  at 10.6 eV could be further established, based on the fact that the sum of the phase-shift fitting values equals  $\pi$  rad.

DOI: 10.1103/PhysRevA.88.012708

PACS number(s): 34.80.Gs

## I. INTRODUCTION

One of the most striking phenomena in the particle scattering experiment is formation of a projectile-target resonance system, namely the projectile with an appropriate energy is temporarily captured and a transient projectile-target complex is formed [1]. Electron-molecule resonance formed in the low-energy electron attachment is classed under such a transient state and described as a discrete state embedded in and interacting with the continuum of the incident electron motion (in terms of Fano's procedure [2]). Different electron-molecule resonant states may be involved in the dissociative electron attachment (DEA), leading to various fragments [3–6]. A lot of efforts have been made to reveal the responsibilities of these resonant states in determination of the total and differential cross sections of the fragments produced in DEA [4–12]. Up to now, there are no experiments explicitly addressing the quantum interference effect on the DEA process. The interference usually tends to be averaged out in the scattering amplitudes in asymptote, because the outgoing dissociative waves initiated from the localized resonant states are believed to be uncorrelated [1]. However, herein the quantum interference is proposed, on the basis of the measurements of the differential cross sections of the anionic fragment  $\text{O}^-$  produced in the DEA process of carbon monoxide (CO).

For a diatomic molecule AB, a typical DEA is  $e^- + \text{AB} \rightarrow (\text{AB})^- \rightarrow \text{A} + \text{B}^-$ , in which the dissociation proceeds through a formation of the resonant state  $(\text{AB})^-$  at an energy of  $E_r$  and with a width of  $\Gamma$ . Normally, two dissociative waves originated from their respective uncorrelated resonant states are localized and develop independently into the asymptotic region [1]. Therefore, if several isolated outgoing waves contribute to the differential cross section of DEA ( $\sigma_{\text{DEA}}$ ), the  $\sigma_{\text{DEA}}$  for the attachment electron with a momentum  $k$  can be simply treated by summation of the individual  $T_{\text{DEA}}^\alpha$  matrix element [12],

$$\sigma_{\text{DEA}} = \sum_{\alpha} (\pi/k) |T_{\text{DEA}}^\alpha|^2. \quad (1)$$

The recently developed ion velocity time-sliced map imaging technique has been successfully applied in elucidation of the intermediate resonant states and dissociation stereodynamics [8–13]. The sliced image of the  $\text{B}^-$  fragment usually shows a specific pattern and thus characterizes the resonant state of certain symmetry. This is achieved under the assumption of localized resonances and by using the Breit-Wigner formula, which seems to be a reasonable hypothesis in light of the theoretical calculations [12]. In general, *complex* resonance patterns are possible as a consequence of the existence of several overlapping resonant states, particularly, when the resonance width is larger than the energy position difference,  $\Gamma(n) > |E_r(n) - E_r(n \pm 1)|$  (Ref. [14]). Consequently, the electron elastic scattering cross sections were found to be remarkably oscillating between these two close-lying resonances [14]. In this work, we show a much more significant effect of the quantum interference on the DEA process of CO. The outgoing dissociative waves propagated from the interfered resonant states lead to the anomalous backward scattering patterns in the sliced images of the  $\text{O}^-$  fragment. The present findings highlight the essentials of quantum interference in the resonant scatterings.

## II. EXPERIMENTAL METHOD

We carried out the DEA experiments for the gas-phase CO molecule in an electron incident energy range of 9.5 ~ 10.6 eV, by using our anion velocity time-sliced map imaging apparatus. The details about this apparatus can be found elsewhere [13]. A top-viewed intersection of the experimental setup is shown in Fig. 1(a). Briefly, an effusive molecular beam of the sample was perpendicular to the pulsed electron beam (with a thermal energy spread of 0.5 eV) which was emitted from a homemade electron gun and collimated with the homogenous magnetic field (~20 Gauss) produced by a pair of Helmholtz coils (not shown). The  $\text{O}^-$  ions produced in the dissociation  $\text{CO}^- \rightarrow \text{C} + \text{O}^-$  were periodically pushed out of the reaction area and then passed through the time-of-flight tube. The  $\text{O}^-$  ions produced in one electron pulse expanded and formed a Newton sphere by the space and velocity focusing [13]. The three-dimensional momentum distribution

\*sxtian@ustc.edu.cn

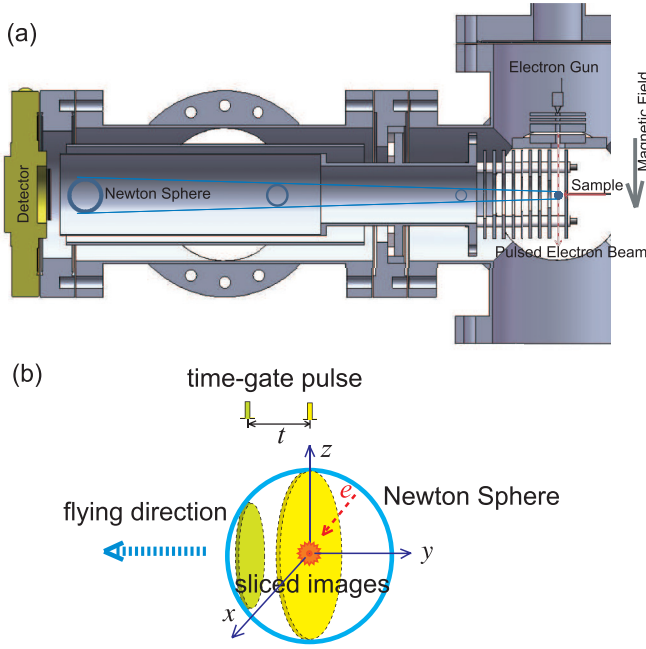


FIG. 1. (Color online) (a) Top-viewed intersection of the anion velocity map imaging apparatus; (b) the experimental principle for recording the time-sliced images.

of the  $O^-$  ions was detected with a pair of microchannel plates and a phosphor screen. The sliced images of  $O^-$  ions were directly recorded with a CCD camera [not shown in Fig. 1(a)].

As shown in Fig. 1(b), we recorded the central time-sliced image (the central sliced sheet of the Newton sphere, denoted as  $t = 0$  ns) by applying a narrow time-gate voltage pulse on the rear microchannel plate; the other sliced images were obtained by putting this pulse ahead or by delaying respective to the central  $t = 0$  ns. In the present experiments, the effective pulse width was about 45 ns, and the ahead-of-time intervals with respect to the central  $t = 0$  ns were 40 and 60 ns. The high-purity gas sample of CO was commercial and no other contaminants were found to disturb the  $O^-$  momentum images.

### III. RESULTS AND DISCUSSION

The sliced images of the  $O^-$  fragment were recorded at the electron energies of 9.5 eV [Fig. 2(a)], 10.0 eV [Fig. 2(b)], and 10.6 eV [Fig. 2(c)]. At 10.6 eV, some  $O^-$  ion signals appear at the center of the image [see the left panel of Fig. 2(c)] but disappear [see the middle and right panels of Fig. 2(c)] when the slicing time gate is moved ahead with 40 and 60 ns. This implies that the kinetic energies of these  $O^-$  ions are near zero eV. In Figs. 2(b) and 2(c), the most significant feature of these images is the backward distribution of the fast  $O^-$  ions. As discussed previously [8–10,12], the momentum distributions of the anionic fragments were closely related to the resonant states of the parent anion formed in the electron attachment.

The complex potential energy curves  $E_{\text{complex}} = E_r - i\frac{\Gamma}{2}$  of  $CO^-$  at the low-lying resonant states have been predicted with the  $R$ -matrix multichannel scattering calculations [15]. In Fig. 3(a), the attachment energies investigated here are

shown with the dotted lines. The thermodynamic threshold of the DEA process  $e^- + CO \rightarrow CO^- \rightarrow C(^3P) + O^-$  is 9.62 eV (Ref. [16]). Four resonant states of  $CO^-$ , i.e., the second  $^2\Pi$ ,  $^2\Delta$ ,  $^2\Phi$ , and  $^2\Sigma$  (see Refs. [15,16]), may be involved in the present study. At the equilibrium bond length of CO ( $R = 2.132 a_0$ ), the second  $^2\Pi$  state as core-excited shape resonance (electron configuration:  $kl\ 1\pi^3 5\sigma^2 2\pi^2$ ) was predicted theoretically at 10.29 eV [15], while assigned at  $9.0 \pm 0.1$  eV ( $\Gamma = 1.2 \pm 0.3$  eV) in the experiment [16];  $^2\Delta$  was also predicted to be a core-excited shape resonance at 9.5 eV [15];  $^2\Phi$ , as another core-excited shape resonance at 10.81 eV, has the width similar to that of the second  $^2\Pi$  state [15]; however, the controversy about the  $^2\Sigma$  state is as follows: a Feshbach resonance at  $E_r = 10.044 \pm 0.01$  eV ( $\Gamma = 0.045 \pm 0.01$  eV) [16] or a core-excited shape resonance at 10.5 eV [15]. The third  $^2\Pi$  state is beyond the present study, due to its too high energy and unphysical feature predicted in Ref. [15]. At 10.6 eV, a small quantity of  $CO^-$  ions at the  $^2\Sigma$  state formed in the vertical attachment may be populated in the potential well [see Fig. 3(a)], subsequently the  $O^-$  ions with the kinetic energies of near zero eV can be produced via the tunneling dissociation. Thus we can observe the  $O^-$  central distributions in the left image of Fig. 2(c). The backward  $O^-$  ions with the higher kinetic energies observed in Figs. 2(b) and 2(c) are attributed to the impulsive dissociations after the vertical transition from the neutral state to the highly repulsive regions of the potential energy curves of  $CO^-$ . According to the reflection principle, the anisotropic momentum distributions of these high-energy  $O^-$  ions [see Figs. 2(b) and 2(c)] should be determined by the intrinsic parities of the resonant states.

Theoretical model for the fragment momentum distributions in the DEA process of diatomic molecule was formulated within the axial-recoil approximation, and the  $\sigma_{\text{DEA}}$  formula was developed as [12]

$$\sigma_{\text{DEA}}(k, \Omega) \propto \sum_{|\mu|} \left| \sum_{l=|\mu|} a_{l\mu} Y_{l\mu}(\theta, \zeta) \right|^2 \approx \sum_{|\mu|} \left| \sum_{j=1, l=|\mu|} c_j e^{i\delta_j} Y_{l\mu}(\theta, \zeta) \right|^2, \quad (2)$$

where  $\Omega$  was the scattering direction of the fragment ion,  $Y_{l\mu}$  was the spherical harmonics,  $a_{l\mu}$  was the energy-dependent expansion coefficient of the incident electron and usually expanded by partial waves with the different angular momenta  $l$  ( $l \geq |\mu|$ ), and  $c_j$  was the weighing parameter of each partial wave.  $|\mu|$  equals  $|\Lambda_f - \Lambda_i|$ , representing the difference in the projection of the angular momentum along the internuclear axis for the neutral ground-state molecule and the resonant-state parent anion. In formation of a resonant state, the different influences on each partial wave of the impinging electron by the interaction potential of the target result in the phase lags ( $\delta_l$ ) among these partial waves. These phase lags also denote the interference of the partial-wave scattering amplitudes for a common resonant state. In practice, the summation of the finite partial waves for a single resonant state (one  $\Lambda_f$  value) and two states (two  $\Lambda_f$  values) in Eq. (2) has been successfully applied in the interpretations of the anionic fragment images [8–10].

Within a single-state model, a transition from the ground state  $^1\Sigma^+(\Lambda_i = 0)$  of the neutral CO to  $^2\Pi(\Lambda_f = 1)$ ,

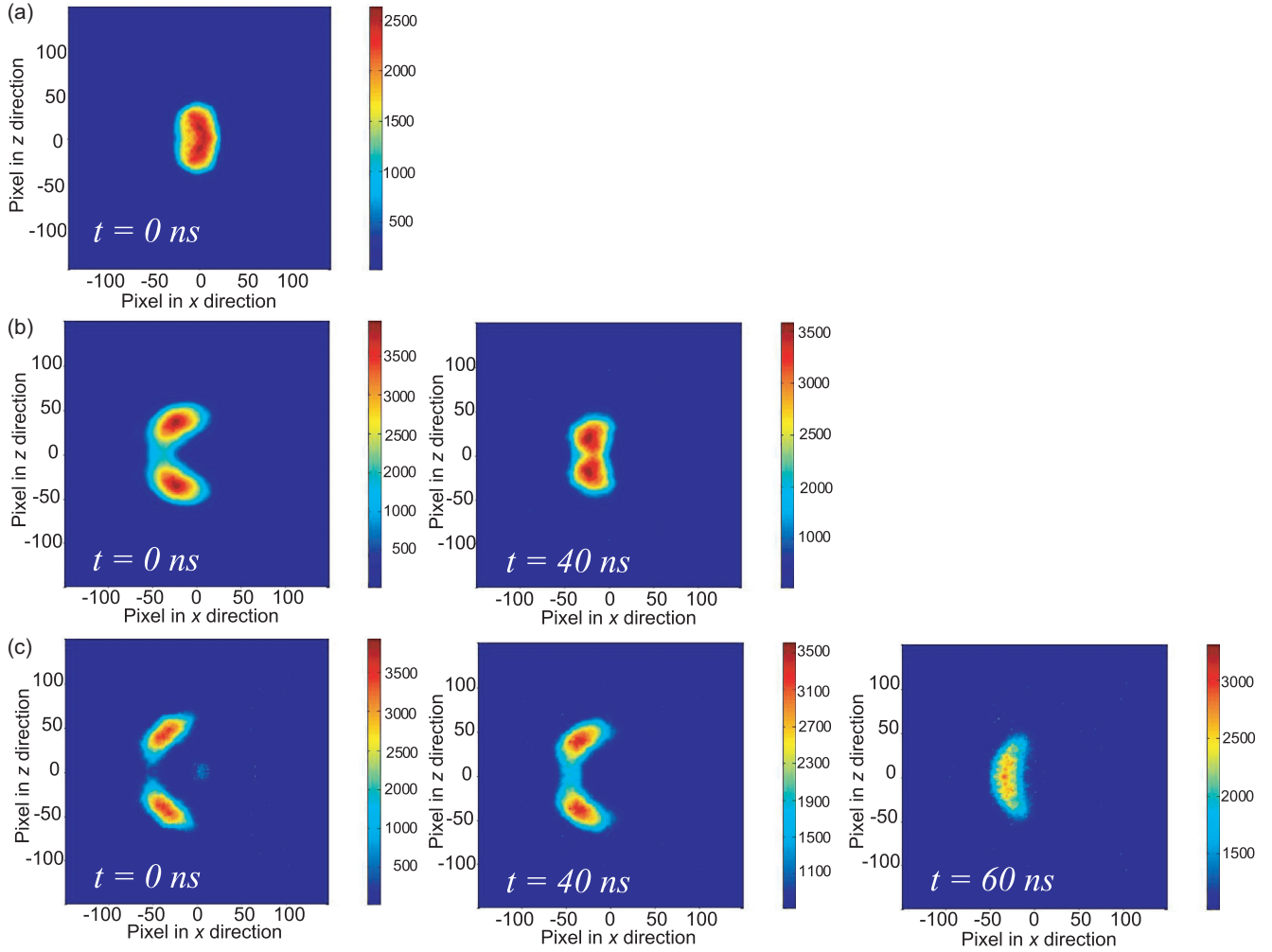


FIG. 2. (Color online) Sliced images of  $O^-$  momentum distribution. The electron incident direction is from left to right. (a) Central sliced image (the reference time at the equatorial plane of Newton sphere,  $t = 0$  ns) recorded at the electron incident energy of 9.5 eV. (b) Sliced images recorded at the electron incident energy of 10.0 eV. (From left to right) The images are obtained at  $t = 0$  ns and  $t = 40$  ns (ahead of time). (c) Sliced images recorded at the electron incident energy of 10.6 eV. (From left to right) The images are obtained at  $t = 0$  ns,  $t = 40$  ns (ahead of time), and  $t = 60$  ns (ahead of time).

${}^2\Delta(\Lambda_f = 2)$ ,  ${}^2\Phi(\Lambda_f = 3)$ , or  ${}^2\Sigma(\Lambda_f = 0)$  resonant state of  $CO^-$  corresponds to the different  $|\mu|$  values of 1, 2, 3, and 0, respectively. For the independent partial waves, i.e., omitting  $\delta_l$ , the angular distributions predicted with Eq. (2) are plotted in Figs. 3(b)–3(e). A common feature of these patterns is the inversion symmetry, namely, all images are in the backward-forward symmetry. If the DEA process experiences two uncorrelated resonant states but leads to the common dissociation products, the  $\sigma_{DEA}(k, \Omega)$  of this two-state model is proportional to a combination (uncorrelated) form,  $|\sum_{j=1} c_j e^{i\delta_j} Y_{l\mu}(\theta, \zeta)|^2 + |\sum_{k=1} c_k e^{i\delta_k} Y_{l\mu}(\theta, \zeta)|^2$ , in which the azimuth angle  $\zeta \approx 0^\circ$  for the central sliced images. As discussed in the following, the distinct backward-scattering pattern of  $O^-$  momentum distributions observed at 10.0 eV [shown in Fig. 2(b)] can be interpreted very well by using this two-state combination mechanism. However, it is out of our expectation that this two-state model, even if more resonant states considered in a multistate model, failed in reproducing the backward-scattering pattern observed at 10.6 eV [see the red line in Fig. 2(c) and the following

discussion]. This can only be interpreted when the interference of the scattering amplitudes is considered.

As shown in Fig. 3(a), the close-lying resonant states in the Franck-Condon region (a shaded arrow) are seriously overlapped, implying that these states are potentially coupled with each other (as the interference of *complex resonances* [14]). Presumably the DEA process experiences these coupling states; we introduce the quantum interference among them to the differential cross section in a straightforward way [17],

$$\sigma_{DEA}(k, \Omega) \propto \sum_{\alpha, \beta} I_{\alpha, \beta} + 2 \sum_{\alpha \neq \beta} \sqrt{I_{\alpha} I_{\beta}} \cos \phi_{\alpha \beta}, \quad (3)$$

where  $I_{\alpha}$  is the amplitude contribution in the form of  $|\sum_{j=1} c_j e^{i\delta_j} Y_{l\mu}(\theta, \zeta)|^2$  for resonant state  $\alpha$ , and  $\phi_{\alpha \beta}$  is the phase shift of the asymptotic waves originated from resonant states  $\alpha$  and  $\beta$ . Equations (1) and (2) represent the summation for the uncorrelated outgoing waves, while Eq. (3) is an interference expression by including the superposition term  $2\sqrt{I_{\alpha} I_{\beta}} \cos \phi_{\alpha \beta}$  and has been successfully used in interpretations to the so-called rainbowlike angular distribution (i.e.,

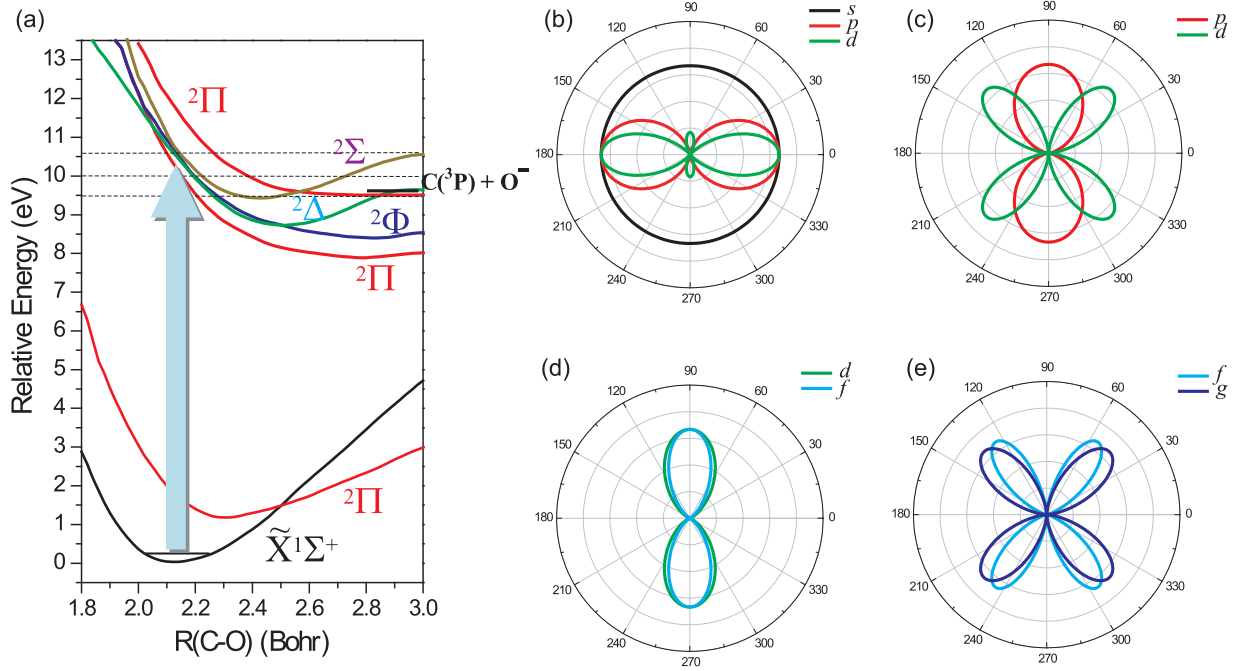


FIG. 3. (Color online) The potential energy curves reproduced from Ref. [15] (a) and the theoretical patterns of the anion angular distributions (b)–(e). (a) The dotted lines indicate the energies investigated in this work; the thick line indicates the thermodynamic threshold of the dissociation to  $C(^3P) + O^-$  (Ref. [16]); the shaded vertical arrow represents the vertical state promotion in the Franck-Condon region. (b)–(e) Show the anion angular distributions of the independent partial waves for the transitions  $1^1\Sigma^+ \rightarrow 2^2\Sigma$ ,  $2^2\Pi$ ,  $2^2\Delta$ , and  $2^2\Phi$ , respectively.  $s$ ,  $p$ ,  $d$ ,  $f$ , and  $g$  denote the respective contributions of the different partial waves (corresponding to  $l = 0, 1, 2, 3, 4$ ) of the incident electron. Each curve is normalized to one at the maximum.

only backward- or forward-scattering distribution observed in the particle scatterings) and quantum interference of different trajectories [17].

After many trial experimental data fittings by using all possible sets of the single-state and multistate (with and without interference) models, the best ones are plotted in Fig. 4 and the fitting parameters are listed in Table I. At the incident energy of 10.0 eV [see Fig. 4(a)], the fitting curves by using the two-state combination [ $I_1 + I_2$  as given in Eq. (2), or excluding the superposition term in Eq. (3)] and its interference expression [ $I_1 + I_2 + 2\sqrt{I_1 I_2} \cos \phi_{12}$  as given in Eq. (3)] for the resonant states  $2^2\Sigma$  ( $I_1 = |c_1 Y_{00} + c_2 e^{i\delta_1} Y_{10} + c_3 e^{i\delta_2} Y_{20}|^2$ ) and the second  $2^2\Pi$  ( $I_2 = |c_4 Y_{11} + c_5 e^{i\delta_3} Y_{21} + c_6 e^{i\delta_4} Y_{31}|^2$ ) are almost the same, and both of them are in excellent agreement

(correlation  $> 0.99$ ) with the experimental data (solid circles). As shown in Table I, the weighing parameter ratio,  $c_1 : c_2 : c_3 : c_4 : c_5 : c_6 = 1 : 0.54 : 0.53 : 0.40 : 0.89 : 0.26$ , indicates that the  $s$  ( $l = 0$ ) and  $d$  ( $l = 2$ ) partial waves are predominant for the  $2^2\Sigma$  and  $2^2\Pi$  states, respectively. The phase shift between two outgoing waves  $|\varphi_{\text{out}}^{(2\Sigma)}\rangle$  and  $|\varphi_{\text{out}}^{(2\Pi)}\rangle$  is  $\phi_{12} = 1.623$  rad. We will not discuss more about the interference among the different partial waves (represented with the phase lags  $\delta_l$ ) for the common resonant state, while the interference of the different resonant states will be stressed. The fitting value 1.623 rad of  $\phi_{12}$  approximately equals  $\pi/2$ , which vanishes the superposition term  $2\sqrt{I_1 I_2} \cos \phi_{12}$  in Eq. (3). Therefore, the destructive interference for the outgoing waves  $|\varphi_{\text{out}}^{(2\Sigma)}\rangle$  and

TABLE I. Fitting parameters obtained by using Eq. (3) for the angular distributions of  $O^-$  produced in the DEA to CO at 10.0 and 10.6 eV.

| Attachment Energy                   | 10.0 eV                         |                                     | 10.6 eV                         |
|-------------------------------------|---------------------------------|-------------------------------------|---------------------------------|
| Weighing ratio                      |                                 |                                     |                                 |
| $c_1 : c_2 : c_3 : c_4 : c_5 : c_6$ | 1: 0.54: 0.53: 0.40: 0.89: 0.26 | $c_1 : c_2 : c_3 : c_4 : c_5 : c_6$ | 1: 0.64: 0.35: 0.29: 0.69: 0.00 |
| Phase lags (rad)                    |                                 |                                     |                                 |
| $(^2\Sigma) \delta_p - \delta_s$    | 2.721                           | $(^2\Pi) \delta_d - \delta_p$       | 3.135                           |
| $\delta_d - \delta_s$               | 3.811                           | $(^2\Delta) \delta_f - \delta_d$    | 5.862                           |
| $(^2\Pi) \delta_d - \delta_p$       | 3.187                           | $(^2\Phi) \delta_g - \delta_f$      | 1.487                           |
| $\delta_f - \delta_p$               | 1.404                           |                                     |                                 |
| Phase shift (rad)                   |                                 |                                     |                                 |
| $\phi_{12} (^2\Sigma - ^2\Pi)$      | 1.623                           | $\phi_{12} (^2\Pi - ^2\Delta)$      | 0.950                           |
|                                     |                                 | $\phi_{31} (^2\Phi - ^2\Pi)$        | 2.570                           |
|                                     |                                 | $\phi_{23} (^2\Delta - ^2\Phi)$     | 2.866                           |

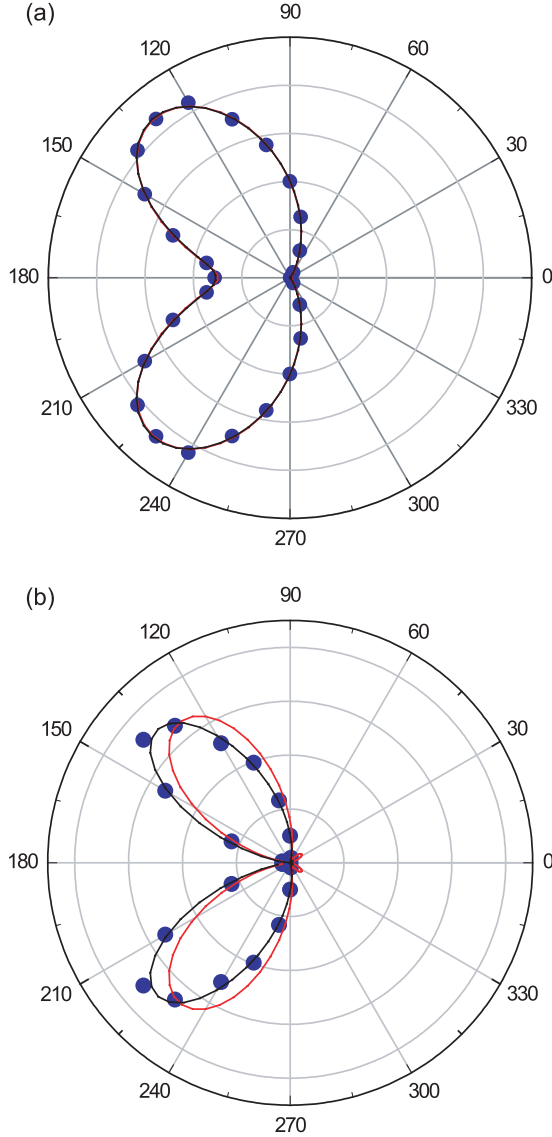


FIG. 4. (Color online) Fitting the experimental angular distributions of the  $O^-$  fragment. The angular distributions (solid circles) of the  $O^-$  fragment are plotted by integration of the ion signals in the selected annular area (corresponding to the kinetic energy range of 0.35–0.65 eV) of the central sliced images [the left of Figs. 1(b) and 1(c)]. At 10.0 eV (a) and 10.6 eV (b), the fitting curves are plotted using the interference (black) and the uncorrelated state combination (red) forms for two (a) and three (b) resonant states.

$|\varphi_{\text{out}}^{(2\Pi)}\rangle$  results in the absence of the forward distribution but the presence of the backward distribution of the  $O^-$  fragment; alternatively, it may be deemed that their corresponding resonant states  $^2\Sigma$  and  $^2\Pi$  are not coupled and the dissociative waves propagate independently into the asymptotic region.

The situation at the incident energy of 10.6 eV is dramatically changed. At least three resonant states should be considered for the better fittings. As shown in Fig. 4(b), after many trial fittings with Eq. (3), we find that the best one consists of  $|c_1 Y_{11} + c_2 e^{i\delta_1} Y_{21}|^2$  ( $I_1$  for the second  $^2\Pi$ ),  $|c_3 Y_{22} + c_4 e^{i\delta_2} Y_{32}|^2$  ( $I_2$  for  $^2\Delta$  state), and  $|c_5 Y_{33} + c_6 e^{i\delta_3} Y_{43}|^2$  ( $I_3$  for  $^2\Phi$  state), together with their superposition terms  $2\sqrt{I_\alpha I_\beta} \cos \phi_{\alpha\beta}$  [ $\alpha, \beta = 1$  (the second  $^2\Pi$ ),  $2$  ( $^2\Delta$ ),  $3$  ( $^2\Phi$ );  $\alpha \neq$

$\beta$ ]. The fitting correlation reaches 0.98. As listed in Table I, the  $p$  ( $l = 1$ ),  $d$  ( $l = 2$ ), and  $f$  ( $l = 3$ ) partial waves are predominant and the relative phase differences or shifts are 0.950 ( $\phi_{12}$ ), 2.570 ( $\phi_{31}$ ), and 2.866 ( $\phi_{23}$ ) rad for the  $^2\Pi$ ,  $^2\Delta$ , and  $^2\Phi$  states, respectively. The superposition terms  $2\sqrt{I_\alpha I_\beta} \cos \phi_{\alpha\beta}$  become significantly important, not only changing the backward-scattering profile but also eliminating two small forward lobes around  $30^\circ$  and  $330^\circ$  of the red fitting curve (obtained with  $I_1 + I_2 + I_3$ ). More interestingly, the interference coherency among the corresponding resonant states can be guaranteed by the phase relationship of  $\phi_{31} + \phi_{12} + \phi_{23} \approx 2\pi$ , where each phase shift  $\phi_{\alpha\beta}$  is obtained independently. The phase sum of  $2\pi$  usually exhibits the maximum visibility of the quantum interference, namely, coherency of the quantum state or wave interference.

Since the target CO molecules in the present experiments are randomly oriented and the dipole moment of the ground-state CO is very small (the negative end is at O atom), the backward scatterings observed in Figs. 2(b) and 2(c) should not be attributed to the attachment preference in a specific target orientation. Although the agreements between the experimental observations and our interference models have been achieved, the more sophisticated calculations, in particular, about the state interference effect on DEA dynamics of this system, are still demanded.

At last, we address the differences between the present observation and the previous measurements by Hall *et al.* [16]. The angular distributions of the  $O^-$  were recorded in the limited range of  $30^\circ \sim 135^\circ$  (Figs. 8 and 9 in Ref. [16]) due to the spatial impediment by using the rotating detector in the turntable arrangement (Fig. 1 in Ref. [16]). Their  $O^-$  angular profiles showed some distributions in the range of  $30^\circ \sim 90^\circ$  (forward direction). Such distinct differences from ours (Fig. 2) can be interpreted as the following: In their measurements, the ion optic lenses and the aperture to collect the  $O^-$  anion were not strictly designed for the spatial and velocity focusing. The reaction area in their experiments was not small enough, and thus the angular correction for the anion collection efficiency was required [16]. The real three-dimensional momentum distribution of the  $O^-$  anion could not be directly measured, in other words, many Newton spheres with the different center positions may exist in the ion flights [16]. In our experiments, the small size (less than  $2 \times 2 \times 2$  mm) of the reaction region and the application of the space and velocity focusing technique only permit one Newton sphere of the  $O^-$  anion in the flight for one pulse [13], which is the key to obtain the clear images. As shown in Fig. 2, all images of the  $O^-$  anion by slicing the Newton sphere at the different positions explicitly show the backward-scattering patterns, and thus any other artificial uncertainties leading to the present observations can be ruled out.

#### IV. CONCLUSION

In summary, we observed the backward-scattering pattern of  $O^-$  momentum distributions at the electron incident energy of 10.6 eV. This may be attributed to coherency of the DEA entrance channel, namely, the attachment to three different resonant states and the coherent redistribution of the population of these states. On the other hand, the backward-scattering

distribution observed at 10.0 eV should be due to a distinctly different entrance channel, in which two orthogonalized resonant states are concerned. More sophisticated theoretical investigation is still needed to gain dynamics about the possible entanglement of resonant states.

#### ACKNOWLEDGMENTS

This work is supported by National Natural Science Foundation of China (Grant No. 21273213), MOST (2011CB921401), and FRFCU.

- 
- [1] J. R. Taylor, *Scattering Theory: The Quantum Theory of Nonrelativistic Collisions* (John Wiley & Sons, New York, 1972).
- [2] U. Fano, *Phys. Rev.* **124**, 1866 (1961).
- [3] L. G. Christophorou, D. L. McCorkle, and A. A. Christodoulides, in *Electron-Molecule Interactions and Their Applications*, edited by L. G. Christophorou (Academic Press, New York, 1984), Vol. 1.
- [4] B. Boudaïfa, P. Cloutier, D. Hunting, M. A. Huels, and L. Sanche, *Science* **287**, 1658 (2000).
- [5] S. Denifl, P. Sulzer, D. Huber, F. Zappa, M. Probst, T. D. Märk, P. Scheier, N. Injan, J. Limtrakul, R. Abouaf, and H. Dunet, *Angew. Chem., Int. Ed.* **46**, 5238 (2007).
- [6] C. König, J. Kopyra, I. Bald, and E. Illenberger, *Phys. Rev. Lett.* **97**, 018105 (2006).
- [7] Y. V. Vasil'ev, B. J. Figard, V. G. Voinov, D. F. Barofsky, and M. L. Deinzer, *J. Am. Chem. Soc.* **128**, 5506 (2006).
- [8] H. Adaniya, B. Rudek, T. Osipov, D. J. Haxton, T. Weber, T. N. Rescigno, C. W. McCurdy, and A. Belkacem, *Phys. Rev. Lett.* **103**, 233201 (2009); **106**, 049302 (2011); N. B. Ram, V. S. Prabhudesai, and E. Krishnakumar, *ibid.* **106**, 049301 (2011).
- [9] N. Bhargava Ram and E. Krishnakumar, *PhysChemChemPhys* **13**, 13621 (2011).
- [10] B. Wu, L. Xia, Y.-F. Wang, H.-K. Li, X.-J. Zeng, and S. X. Tian, *Phys. Rev. A* **85**, 052709 (2012).
- [11] Y. F. Wang and S. X. Tian, *PhysChemChemPhys* **13**, 15597 (2011); *Phys. Rev. A* **85**, 012706 (2012).
- [12] T. F. O'Malley, *Phys. Rev.* **150**, 14 (1966); T. F. O'Malley and H. S. Taylor, *ibid.* **176**, 207 (1968); H. Klar and H. Morgner, *J. Phys. B* **12**, 2369 (1979).
- [13] B. Wu, L. Xia, H.-K. Li, X.-J. Zeng, and S. X. Tian, *Rev. Sci. Instrum.* **83**, 013108 (2012).
- [14] F. H. Mies, *Phys. Rev.* **175**, 164 (1968); E. Narevicius, and N. Moiseyev, *Phys. Rev. Lett.* **84**, 1681 (2000).
- [15] L. A. Morgan and J. Tennyson, *J. Phys. B* **26**, 2429 (1993).
- [16] R. I. Hall, I. Čadež, C. Schermann, and M. Tronc, *Phys. Rev. A* **15**, 599 (1977); J. Comer and F. H. Read, *J. Phys. B* **4**, 1678 (1971).
- [17] R. D. Levine, *Molecular Reaction Dynamics* (Cambridge University Press, New York, 2005).